

SHARP ECCENTRIC RINGS IN PLANETLESS HYDRODYNAMICAL MODELS OF DEBRIS DISKS.

WLADIMIR LYRA^{1,2,3} AND MARC J. KUCHNER⁴

Draft version

ABSTRACT

Debris disks should not be completely gas-free, since there is second generation gas from outgassing of planetesimals and dust grains via sublimation, photodesorption, or collisions, generating a system of dust-to-gas ratio close to unity, where hydrodynamics cannot be ignored. A clumping instability exists in this configuration, that has been hitherto explored only in one-dimensional, incompressible models. We performed 2D numerical compressible models of a disk with comparable amounts of gas and dust to study the growth and development of this instability. Our model solves the momentum equation for the gas and dust, together with energy and continuity equations. We uncover that the backreaction of the drag force from the gas onto the dust shepherds rings, similar to those observed in debris disks and usually attributed to the presence of hypothetical undetected planets. We also uncover that the eccentricity of these rings, usually presented as convincing evidence for the presence of a planet, can actually be simply explained by a standing wave propagating along the ring. The rings support a spectrum of oscillations, with one particular mode representing epicyclic motion. The apparent eccentricity matches the eccentricity in observed systems. This suggests that the planet possibility, though thrilling, is not necessarily required to explain these systems.

1. INTRODUCTION

Disks around young stars appear to pass through an evolutionary phase when the disk is optically-thin and the dust to gas ratio is of order unity give or take an order of magnitude. It can be hard to precisely measure the total masses of the dust and gas in such disks, but the nearby stars β Pictoris (Lagrange et al. 1998; Olofsson et al. 2001; Brandeker et al. 2004; Roberge et al. 2006; Troutman et al. 2011), HD32297 (Redfield 2007), 49 Ceti (Zuckerman et al. 1995) and HD 21997 (Moor et al. 2011) all host disks of dust resembling ordinary debris disks and also have stable circumstellar gas detected in molecular CO, Na I or other metal lines; the inferred mass of gas ranges from Lunar masses to a few Earth masses. The gas in these disks is thought to be produced by planetesimals or dust grains themselves, via sublimation or photodesorption (Gregorieva et al. 2007) or collisions (Czechowski & Mann 2007), processes that should occur in every debris disk at some level.

This kind of disk may form rings, clumps, or spiral structures via a recently proposed instability (Klahr & Lin 2005; Besla & Wu 2007) that is the subject of this paper. Under a wide range of conditions, gas drag causes dust in a gas disk to concentrate at pressure maxima in the disk (Takeuchi & Artymowicz 2001). But when the disk is optically-thin to starlight, the gas is most likely primarily heated by the dust, via photoelectric heating. In this circumstance, a concentration of dust that heats the gas creates a local pressure maximum that in turn can cause the dust to concentrate more.

The result of this instability could be that the dust and gas clump into rings or spiral patterns or other structures that could be detected via coronagraphic imaging or other methods. Indeed, images of debris disks and transitional disks show a range of asymmetries and other structures that beg for explanation. Klahr & Lin (2005) raised the possibility that the instability they hypothesized could explain some of the observed structures. Alternative explanations for these structures sometimes rely on planetary perturbers—a tantalizing possibility. But we are interested in investigating any possible explanation for these disk structures that does not require a hidden planetary companion.

More investigation of this instability is needed. Previous investigations of the instability neglected a crucial aspect of the disk dynamics: the momentum equation for the dust and gas. In other words, they effectively ignored the inertia of the dust and gas, a property that could damp the growth of the instability, or otherwise fundamentally alter it. Moreover, prior investigations only considered one-dimensional models, which can only investigate azimuthally-symmetric, ring-like patterns. This limitation also left open the possibility that in higher dimensions, the power in the instability might collect in higher azimuthal wavenumbers, generating only small clumps that would be unobservable. Such behavior would make this instability uninteresting as an explanation for the structures seen in circumstellar disks.

To deepen our understanding of this instability, we performed a 2-D numerical and analytic investigation of a disk containing comparable masses of gas and dust. Our model solves the momentum equation for the gas and dust, together with energy and continuity equations, an improvement over prior models. We report on the parameter space where this stability grows (dust-to-gas ratio, thermal and coupling times). Finally, we discuss the possibility that this instability could result in

wlyra@jpl.nasa.gov, marc.j.kuchner@nasa.gov

¹ Department of Astrophysics, American Museum of Natural History, 79th Street at Central Park West, New York, NY, 10024, USA

² Jet Propulsion Laboratory, California Institute of Technology, 4800 Oak Grove Drive, Pasadena, CA, 91109, USA

³ NASA Carl Sagan Fellow

⁴ NASA Goddard Space Flight Center, Exoplanets and Stellar Astrophysics Laboratory, Code 667, Greenbelt, MD 21230, USA

detectable structures in transitional disks or debris disks with gas.

2. THE PHYSICAL REGIME

Debris disks with gas represent a regime of nebular astrophysics that has only recently been quantified. The archetype of the class, the best studied object so far, is the disk around β Pictoris. Zagorovsky et al. (2010) have assembled a model for the properties of this disk that we will use as a reference point for our study.

It is important to note that the total mass of gas that these debris disks have is poorly known, even for the well-studied disk around β Pictoris. Debris disk gas has mainly been observed in emission lines from metal ions and CO, but the bulk of the gas is generally assumed to be hydrogen, a component that is difficult to measure (See e.g. Thi et al. 2001). Estimates of the hydrogen abundance in the β Pictoris disk relative to the solar value range from 10^{-3} to 1; this range translates into a range of total gas mass from about $8 \times 10^{-4} M_{\oplus}$ to $0.8 M_{\oplus}$.

The dust mass is better constrained. Still, care must be taken to specify the particle size range of interest, since in typical grain size distributions, the larger bodies contain most of the mass, yet the smaller grains are the ones that we can detect. Zagorovsky et al. (2010) quote a dust mass of $0.27 M_{\oplus}$ for particles smaller than 1 cm, assuming spherical grains with a number distribution $dn/ds \propto s^{-3.5}$, where s is the grain radius. Let us call the dust-to-gas ratio ε . Given these numbers, ε for β Pictoris would lie in the range of 0.3 to 300.

These numbers roughly span the range of parameters for other debris disks with gas, with 49 Ceti a notably gas-rich exception. (Moor et al. 2011) estimate that the HD 21997 disk has a dust mass of $\sim 0.1 M_{\oplus}$ and a gas mass of $0.35 M_{\oplus}$, corresponding to $\varepsilon \approx 0.3$. (Redfield 2007) estimates an upper limit to the gas mass for HD 32297 of $\sim 0.3 M_{\oplus}$; (Maness 2008) find that the dust mass in this system is in the range of 0.02 – $1 M_{\oplus}$, yielding ε in the range ≈ 0.05 – 3 . The 49 Ceti debris disk has about the same mass of dust as HD21997, but substantially more gas: $13 M_{\oplus}$ (Zuckerman et al. 1995), corresponding to $\varepsilon \approx 0.008$.

Another important quantity for the instability we investigated is the thermal time scale. In the Zagorovsky et al. (2010) model (the " β Pictoris" model, not the "fiducial" model), the dust is concentrated in a ring about 100–140 AU from the star. At the peak in the dust density, the midplane gas density is about 10 cm^{-3} , the dust temperature is roughly 100 K, the gas temperature is roughly 70 K. The gas is primarily heated by photoelectric emission from dust grains, and primarily cooled through the C II 157.7 μm line emission and the total heating/cooling power is roughly $2 \times 10^{-19} \text{ erg s}^{-1} \text{ cm}^{-3}$. Since the specific heat of molecular hydrogen at 70 K is roughly $1.3 \times 10^8 \text{ erg g}^{-1} \text{ K}^{-1}$, the thermal time scale in this model is about $0.5(n/10 \text{ cm}^{-3})$ years, where n is the midplane H_2 number density. Given the range of possible hydrogen abundances in the disk, the range of time scales of interest corresponds to about 10^{-4} to 0.1 orbital periods.

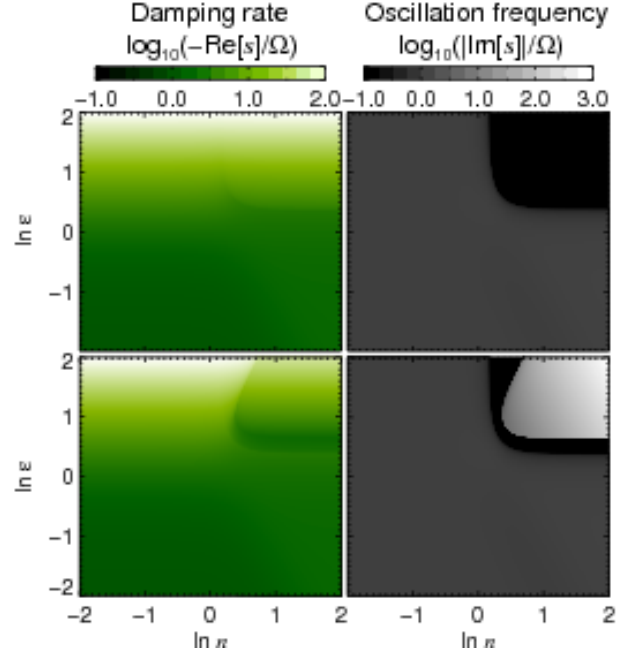


FIG. 1.— Two of the five solutions of Eq. (32), corresponding to damped oscillations through most of the parameter space. In a small region (high dust-to-gas ratio and high frequency) modes are exponentially damped without oscillating. The other three solutions Fig. 2 involve linear growth.

3. THE MODEL

We work primarily in the thin disk approximation, using the vertically integrated equations of hydrodynamics

$$\frac{\partial \Sigma_g}{\partial t} = -(\mathbf{u} \cdot \nabla) \Sigma_g - \Sigma_g \nabla \cdot \mathbf{u} \quad (1)$$

$$\frac{\partial \mathbf{u}}{\partial t} = -(\mathbf{u} \cdot \nabla) \mathbf{u} - \frac{1}{\Sigma_g} \nabla P - \nabla \Phi - \frac{\Sigma_d}{\Sigma_g} \mathbf{f}_d \quad (2)$$

$$\frac{\partial S}{\partial t} = -(\mathbf{u} \cdot \nabla) S - \frac{c_v}{T} \frac{(T - T_p)}{\tau_r}. \quad (3)$$

In these equations, Σ_g and Σ_d are the vertically integrated gas and dust densities, respectively; \mathbf{u} stands for the velocity of the gas parcels, P is the pressure, and Φ is the gravitational potential. $S = c_v (\ln P - \gamma \ln \Sigma_g)$ is the gas entropy, where c_v is the specific heat at constant volume and $\gamma = c_p/c_v$ is the adiabatic index, with c_p the heat capacity at constant pressure. T stands for the gas temperature.

The dust evolves Lagrangianly according to

$$\frac{d\mathbf{x}}{dt} = \mathbf{v} \quad (4)$$

$$\frac{d\mathbf{v}}{dt} = -\nabla \Phi + \mathbf{f}_d \quad (5)$$

where \mathbf{x} is the position of a dust particle and \mathbf{v} its velocity. The gravitational potential is given by $\Phi = -GM_*/r^2$, where G is the gravitational constant, M_* the stellar mass, and r the stellocentric distance. For the

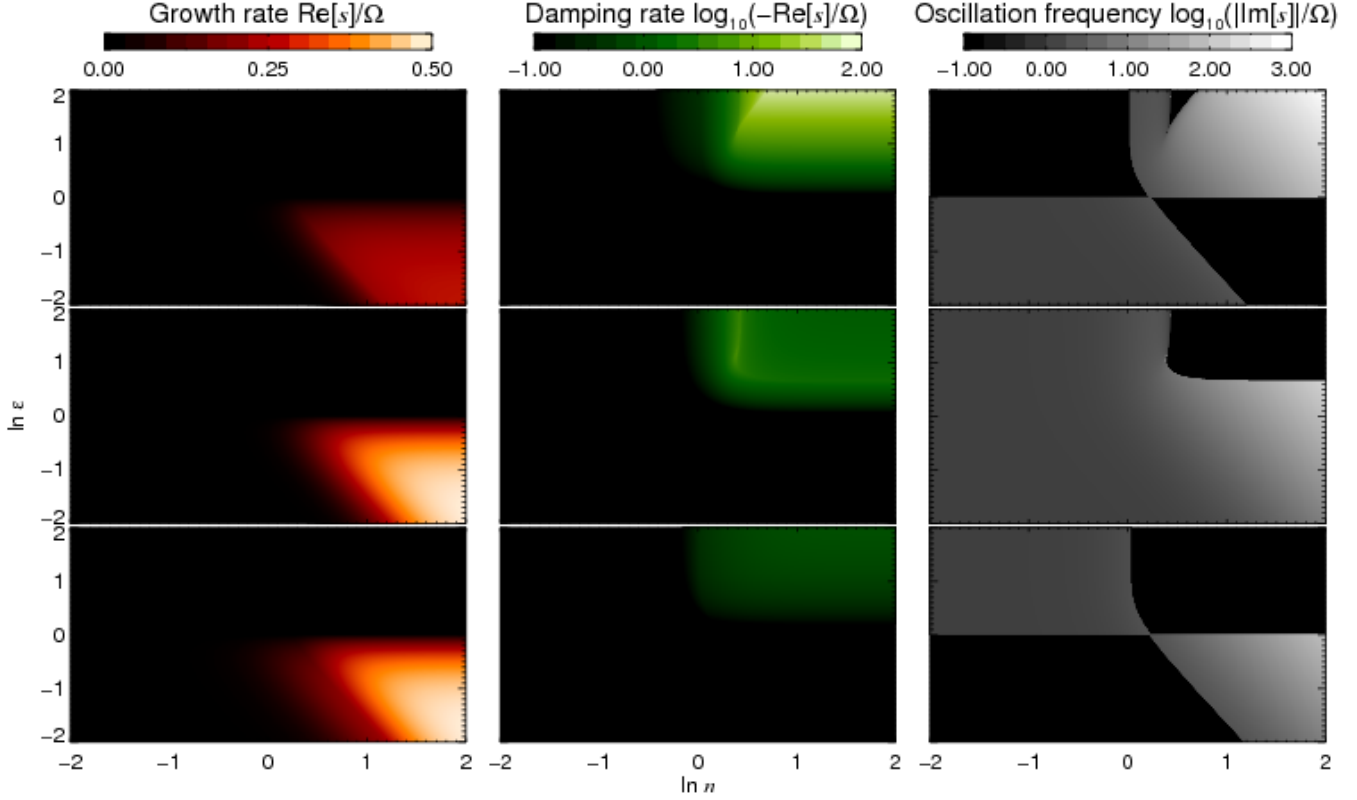


FIG. 2.— The three of the five solutions of Eq. (32) that show linear growth. Growth is restricted to the low dust-to-gas ratio ($\varepsilon < 1$), high wavenumber ($n > 1$) region of parameter space. The growing modes in the solutions shown in the middle and lower panels have non-zero associated oscillation frequencies – an overinstability. Conversely, the solution shown in the upper panel is a true instability.

pressure we use the ideal gas law $P = \Sigma_g c_s^2 / \gamma$, where c_s is the sound speed.

The model is closed by specifying the drag force f_d by which gas and dust interact; and T_p , a simple prescription for the gas temperature set by photoelectric heating. These are given by

$$f_d = -\frac{(v - u)}{\tau_f} \quad (6)$$

$$T_p = T_0 \frac{\Sigma_d}{\Sigma_0}. \quad (7)$$

The quantities τ_f and τ_T are the dynamical and thermal coupling times between gas and dust, respectively. They have a radial variance to match the Keplerian rate

$$\tau_f = \tau_{f0} \Omega_0 / \Omega \quad (8)$$

$$\tau_T = \tau_{T0} \Omega_0 / \Omega \quad (9)$$

where $\Omega = \sqrt{GM_\star / r^3}$ is the Keplerian angular frequency. The quantities τ_{f0} and τ_{T0} are free parameters of the model.

Given that the thermal time is sometimes expected to be very low (10^{-4} orbital periods as estimated in Sect. 2), we also run models with instantaneous thermal coupling. For these models, we skip solving the energy equation, and equate $T = T_p$ according to Eq. (7). The

sound speed is updated accordingly. This change effectively amounts to choosing a new equation of state that depends on the dust density.

$$\lim_{\tau_T \rightarrow 0} P = c_v (\gamma - 1) T_0 \Sigma_g \Sigma_d / \Sigma_0. \quad (10)$$

We solve the equations with the PENCIL CODE⁵ which integrates the evolution equations with sixth order spatial derivatives, and a third order Runge-Kutta time integrator. Sixth-order hyperdissipation terms are added to Eq. (1)-Eq. (3), to provide extra dissipation near the grid scale, explained in Lyra et al. (2008, 2009). They are needed because the high order scheme of the Pencil Code has little overall numerical dissipation (McNally et al. 2012).

4. LINEAR STABILITY ANALYSIS

We start by performing a linear stability analysis, that should assist on interpreting the results of the numerical simulations. To derive the perturbation equations, we make use of the shearing sheet and fluid approximations. The first treats the equations in a local, co-rotating Cartesian frame. The second greatly simplifies the treatment of solid particles by having a continuity equation. The 2D equations are

⁵ The code, including improvements done for the present work, is publicly available under a GNU open source license and can be downloaded at <http://www.nordita.org/software/pencil-code>

$$\mathcal{D}_v \Sigma_d = -\Sigma_d \nabla \cdot \mathbf{v} \quad (11)$$

$$\mathcal{D}_v v_x = 2\Omega v_y - \frac{1}{\tau_f}(v_x - u_x) \quad (12)$$

$$\mathcal{D}_v v_y = -\frac{1}{2}\Omega v_x - \frac{1}{\tau_f}(v_y - u_y) \quad (13)$$

$$\mathcal{D}_u \Sigma_g = -\Sigma_g \nabla \cdot \mathbf{u} \quad (14)$$

$$\mathcal{D}_u u_x = 2\Omega u_y - \frac{1}{\Sigma_g} \frac{\partial P}{\partial x} - \frac{\varepsilon}{\tau_f}(u_x - v_x) \quad (15)$$

$$\mathcal{D}_u u_y = -\frac{1}{2}\Omega u_x - \frac{1}{\Sigma_g} \frac{\partial P}{\partial y} - \frac{\varepsilon}{\tau_f}(u_y - v_y) \quad (16)$$

where $\varepsilon = \Sigma_d/\Sigma_g$ is the dust-to-gas ratio and

$$\mathcal{D}_w = \partial_t + \mathbf{w} \cdot \nabla - q\Omega x \partial_y \quad (17)$$

is the shear-modified advective derivative, with $q = 3/2$ the Keplerian shear rate. Upon linear decomposition $\psi = \psi_0 + \psi'$ and considering axis-symmetric planar wave perturbations $\psi' = \hat{\psi} \exp(st + ikx)$, these equations become

$$s \hat{\Sigma}_d = -\Sigma_{d0} ik \hat{v}_x \quad (18)$$

$$s \hat{v}_x = 2\Omega \hat{v}_y - \frac{1}{\tau_f}(\hat{v}_x - \hat{u}_x) \quad (19)$$

$$s \hat{v}_y = -\frac{1}{2}\Omega \hat{v}_x - \frac{1}{\tau_f}(\hat{v}_y - \hat{u}_y) \quad (20)$$

$$s \hat{\Sigma}_g = -\Sigma_{g0} ik \hat{u}_x \quad (21)$$

$$s \hat{u}_x = 2\Omega \hat{u}_y - \mathcal{C} ik (\hat{\Sigma}_d + \varepsilon \hat{\Sigma}_g) - \frac{\varepsilon}{\tau_f}(\hat{u}_x - \hat{v}_x) \quad (22)$$

$$s \hat{u}_y = -\frac{1}{2}\Omega \hat{u}_x - \frac{\varepsilon}{\tau_f}(\hat{u}_y - \hat{v}_y) \quad (23)$$

where we used the instantaneous thermal coupling approximation (Eq. 10) to substitute

$$\nabla P = \mathcal{C}(\Sigma_g \nabla \Sigma_d + \Sigma_d \nabla \Sigma_g), \quad (24)$$

with $\mathcal{C} = c_v(\gamma - 1)T_0/\Sigma_0 = c_{s0}^2/(\gamma\Sigma_0)$. Equations (18) and (21) readily allow for reducing the system to only four equations. We substitute these in the radial equation for gas velocity to obtain

$$s \hat{v}_x = 2\Omega \hat{v}_y - \frac{1}{\tau_f}(\hat{v}_x - \hat{u}_x) \quad (25)$$

$$s \hat{v}_y = -\frac{1}{2}\Omega \hat{v}_x - \frac{1}{\tau_f}(\hat{v}_y - \hat{u}_y) \quad (26)$$

$$s \hat{u}_x = 2\Omega \hat{u}_y - \varepsilon \left(\frac{1}{\tau_f} + \frac{iN^2}{s} \right) \hat{u}_x + \varepsilon \left(\frac{1}{\tau_f} - \frac{iN^2}{s} \right) \hat{v}_x \quad (27)$$

$$s \hat{u}_y = -\frac{1}{2}\Omega \hat{u}_x - \frac{\varepsilon}{\tau_f}(\hat{u}_y - \hat{v}_y) \quad (28)$$

where we also substituted

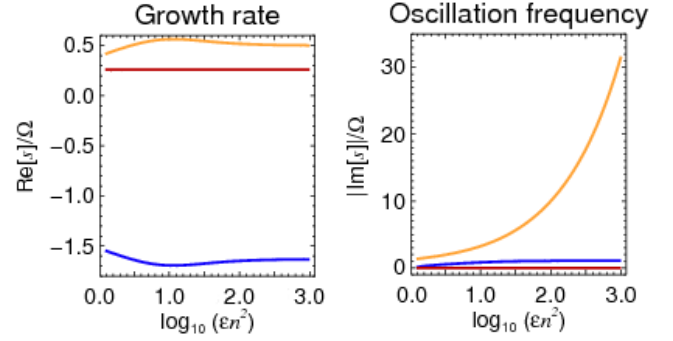


FIG. 3.— Using $x = \varepsilon n^2$ and taking the limit $x \gg 1$ allows for better visualizing the three behaviours: true instability (red), overstability (dark yellow), and damped oscillations (blue). The other two solutions are the complex conjugate of the oscillating solutions, and not shown.

$$N^2 = k^2 c_{s0}^2 \Sigma_{g0} / (\gamma \Sigma_0). \quad (29)$$

We now substitute $\tau_f = 1/\Omega$ so that the dispersion relation becomes simpler yet still captures the physically interesting case of the most mobile dust. Non-dimensionalizing $\omega = s/\Omega$, $n = N/\Omega$ we solve the eigenvalue problem

$$(\mathbf{M} - \mathbf{I}\omega) \cdot \boldsymbol{\sigma} = 0 \quad (30)$$

where $\boldsymbol{\sigma} = (\hat{v}_x, \hat{v}_y, \hat{u}_x, \hat{u}_y)^T$, \mathbf{I} is the unit matrix, and

$$\mathbf{M} = \begin{bmatrix} -1 & 2 & 1 & 0 \\ -1/2 & -1 & 0 & 1 \\ \varepsilon(1 - n^2/\omega) & 0 & -\varepsilon(1 + n^2/\omega) & 2 \\ 0 & \varepsilon & -1/2 & -\varepsilon \end{bmatrix}. \quad (31)$$

The dispersion relation for this linear system is a quintic polynomial

$$A\omega^5 + B\omega^4 + C\omega^3 + D\omega^2 + E\omega + F = 0 \quad (32)$$

with coefficients

$$A = 1, \quad (33)$$

$$B = 2\varepsilon + 2, \quad (34)$$

$$C = \varepsilon^2 + \varepsilon(n^2 + 2) + 3, \quad (35)$$

$$D = \varepsilon^2 n^2 + \varepsilon(3n^2 + 2) + 2, \quad (36)$$

$$E = \varepsilon^2(2n^2 + 1) + \varepsilon(3n^2 + 2) + 2, \quad (37)$$

$$F = \varepsilon^2 n^2 - \varepsilon n^2. \quad (38)$$

We explore the solutions of the system in the next sections.

4.1. Growth

Eq. (32) has five solutions. Since quintics do not have a complete analytical solution, we solve it numerically at first, to explore the behaviour of the solutions. Since we considered planar wave modes of form $\exp(st + ikx)$, the imaginary part of the complex root means oscillations, whereas the real positive (negative) part translates into exponential growth (damping).

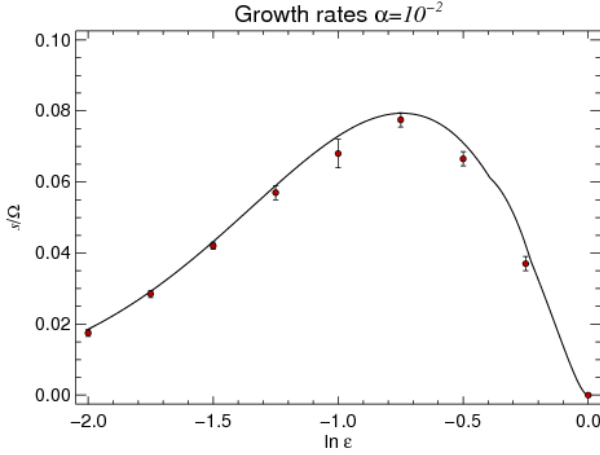


FIG. 4.— The analytical prediction (Eq. 41) of the linear instability growth compared to the growth rates measured numerically. The overall agreement is excellent. The growth rates are only very slightly underestimated.

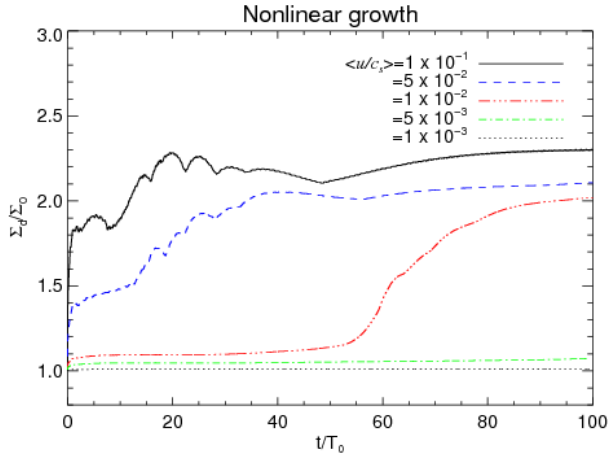


FIG. 5.— Although there is no linear instability for $\varepsilon = 1$, growth occurs when the amplitude of the initial perturbation is increased. The saturation level also depends on the strength of the initial perturbation. These are hallmarks of nonlinear instability.

Two of the solutions do not have unstable linear modes, representing damped oscillations (Fig. 1). We plot in Fig. 2 the three solutions that do show linear growth, as a function of the dust-to-gas ratio ε and the normalized wavenumber n . The left panels show the growth rates, the middle ones the damping rates, and the right panels the oscillation frequency of the modes.

The solutions show that there is no linear growth for $\varepsilon \geq 1$. No growth occurs for $n \leq 1$ either. The linear instability is restricted to the phase space $n > 1$, $\varepsilon < 1$ only. At low dust load and high wavenumber the three growing modes appear. The growing modes in the upper panel have zero oscillation frequency, characterizing a true instability. As for the two other growing solutions, the associated non-zero oscillation frequencies make them overstabilities. The pattern of larger growth rates at large n and low ε invites to explore the limit $n \gg 1$ and $\varepsilon \ll 1$. We thus take $x = \varepsilon n^2$ as characteristic variable, and explore the behaviour of $x \gg 1$. In this

approximation, the coefficients are

$$\begin{aligned} A &= 1; & B &= 2; & C &= x; \\ D &= 3x; & E &= 3x; & F &= -x. \end{aligned} \quad (39)$$

The solutions are plotted in Fig. 3. The instability is plotted as the red line. The growth rate is $\Omega/4$ for all x . The overstability is plotted as the dark yellow line. It reaches an asymptotic growth rate of $\Omega/2$, at ever growing oscillation frequencies. Damped oscillations at the epicyclic frequency show as the blue line. The other two roots are the complex conjugate of the damped and overstable solutions, and not shown.

4.2. Long wavelength limit - undamped oscillations

Of particular interest are the free, undamped, oscillation that occur through most of the parameter space of Fig. 2. We can find these modes analytically by taking the long wavelength limit ($n \rightarrow 0$). Ignoring the n terms, the system becomes a quartic equation,

$$\begin{aligned} A &= 1; & B &= 2\varepsilon + 2; & C &= \varepsilon^2 + 2\varepsilon + 3; \\ D &= 2\varepsilon + 2; & E &= \varepsilon^2 + 2\varepsilon + 2; & F &= 0; \end{aligned}$$

which can be solved exactly. The roots are

$$\lim_{n \rightarrow 0} \omega = \pm i; \quad \lim_{n \rightarrow 0} \omega = -(\varepsilon + 1) \pm i \quad (40)$$

i.e., two solutions are undamped oscillations at wave frequency Ω , thus constituting epicyclic oscillations. The other two solutions are damped oscillations at the same frequency Ω , and damping time $(\varepsilon + 1)\Omega^{-1}$. The eigenvector corresponding to the $\varpi = \pm 1$ solution represent the particular mode for which $\hat{v}_x = \hat{u}_x$ and $\hat{v}_y = \hat{u}_y$, therefore canceling the drag force. This epicyclic mode is low- k and undamped, and should show up in the simulations as a standing wave. We will go back to this mode in the next sections.

5. NONLINEAR NUMERICAL SIMULATIONS

5.1. Comparing linear theory and simulations

From the solutions, we see that there is significant growth even for very small wavenumbers. The simulations, however, will cap power at and near the grid scale. To make for a meaningful comparison, we add artificial Laplacian viscosity ν to the gas and dust momentum equations. The extra term in Fourier space is proportional to νk^2 , which, using the alpha-viscosity recipe of Shakura & Sunyaev (1963) $\nu = \alpha c_s H$, normalizing by Ω , and substituting Eq. (29), reduces to $q = \alpha \gamma n^2$. This enters in the coefficient matrix as diagonal terms. The new, viscous, system is therefore

$$[\mathbf{M} - \mathbf{I}(\omega + q)] \cdot \boldsymbol{\sigma} = 0 \quad (41)$$

We set $\alpha = 10^{-2}$ and solve the system numerically. A comparison between the predicted and measured linear growth rates is shown in Fig. 4. The agreement is excellent, with the measured growth rates only very slightly systematically offset from the analytical prediction.

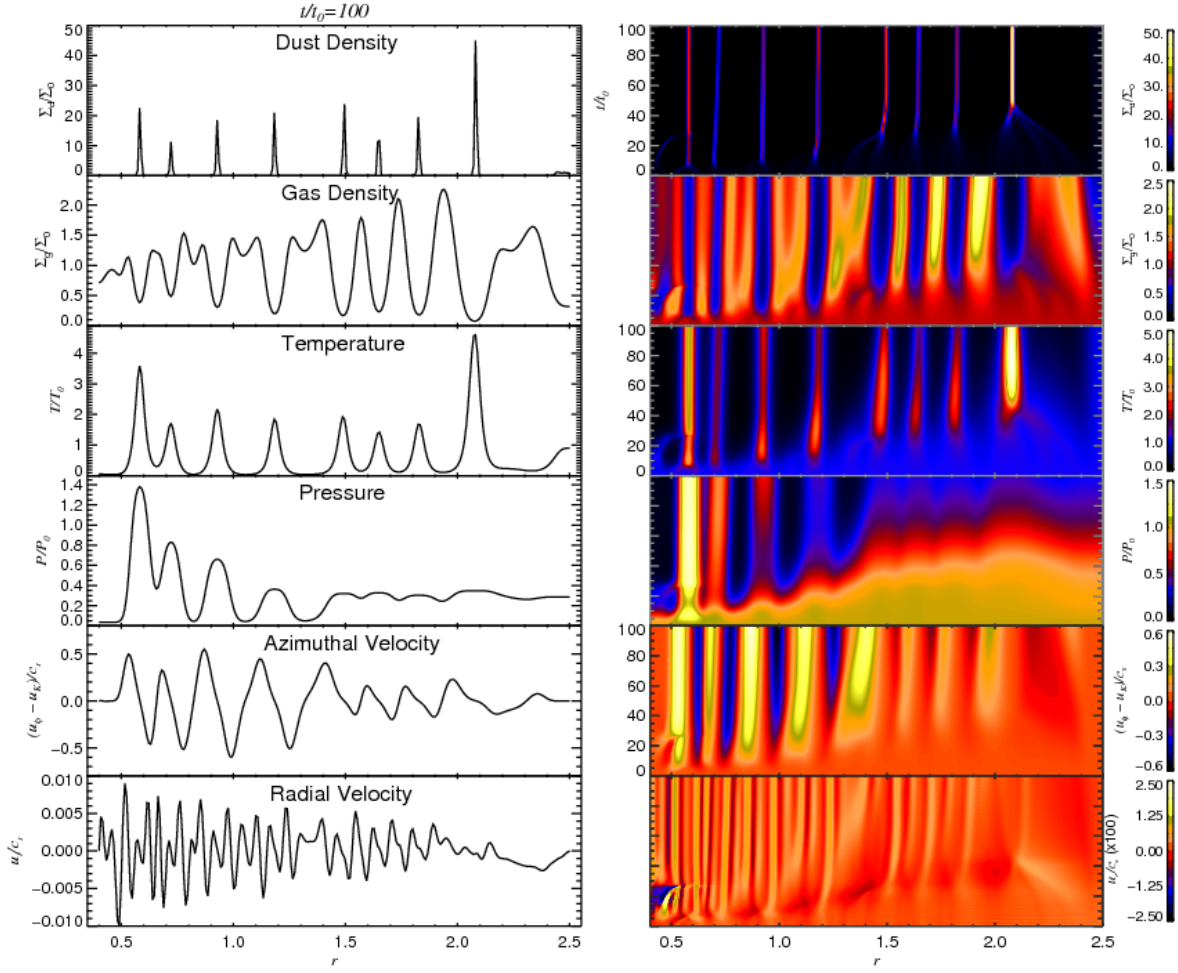


FIG. 6.— End state (left panels) and time evolution (right panels) of the heating instability in one dimension. The photoelectric heating associated with the dust generates pressure maxima at the location of dust, that in turn attracts more dust via the drag force. The heating of the gas leads to its expansion; the instability maintains a spatial segregation between the gas and the dust. The model shown has $\tau_{f0} = 1$, for the most mobile dust, and $\tau_{T0} = 2\pi$.

5.2. Nonlinear growth

As seen from Figs. 2 and 4, there is no linear growth at $\varepsilon = 1$ and beyond, so any growth in this regime must be nonlinear. Indeed, nonlinear growth is seen to occur for $\varepsilon = 1$ when we raise the noise amplitude from 10^{-3} to 10^{-1} (Fig. 5). The growth rate and saturation value increase with increasing amplitude of the initial perturbation, as expected for subcritical instabilities (e.g. Lesur & Papaloizou 2010; Lyra & Klahr 2011).

5.3. Numerical results

We model a two-dimensional disk on a uniformly spaced grid in cylindrical coordinates (r, ϕ) , ranging $r=[0.5, 1.5]r_0$ and $\phi=[-\pi, \pi]$. We run models with resolution $[N_r, N_\phi]=[256, 256]$. The units are such that

$$GM_\star = r_0 = \Omega_0 = \Sigma_0 = c_p = 1 \quad (42)$$

To isolate the effect of heating, we shut down migration of particles by using initially constant density and temperature. The sound speed is set at $c_{s0}=0.1$, and the adiabatic index $\gamma = 1.4$. The reference temperature

is $T_0 = c_{s0}^2/[c_p(\gamma - 1)]$. Substituting the values, we get $T_0 = 2.5 \times 10^{-2}$ in code units.

We use numerical particles to represent the dust phase of the disk, with initially ten particles per grid point, so a total of $N_p = 10 \times 256^2 = 655360$ numerical particles. These are initially placed in circular Keplerian orbits. The dust-to-gas ratio is set to unity.

We use reflective boundaries with a buffer zone of width 0.1 in each radial border that drives the quantities to the initial condition at a dynamical timescale. We use outflow no-inlet boundary conditions for the radial velocity, constant gradient for the azimuthal velocity, and zero gradient for density and entropy. The simulations are usually run for one hundred orbits at r_0 .

5.3.1. The instability in one dimension

To understand the nature of the instability, it is instructive to consider it first in one-dimensional models, since it allows a more thorough exploration of the parameter space. We also shut down the drag force backreaction, in order to better isolate the effect of heating (but as we show later, this term will become of paramount importance in the phenomenology of debris disks in the

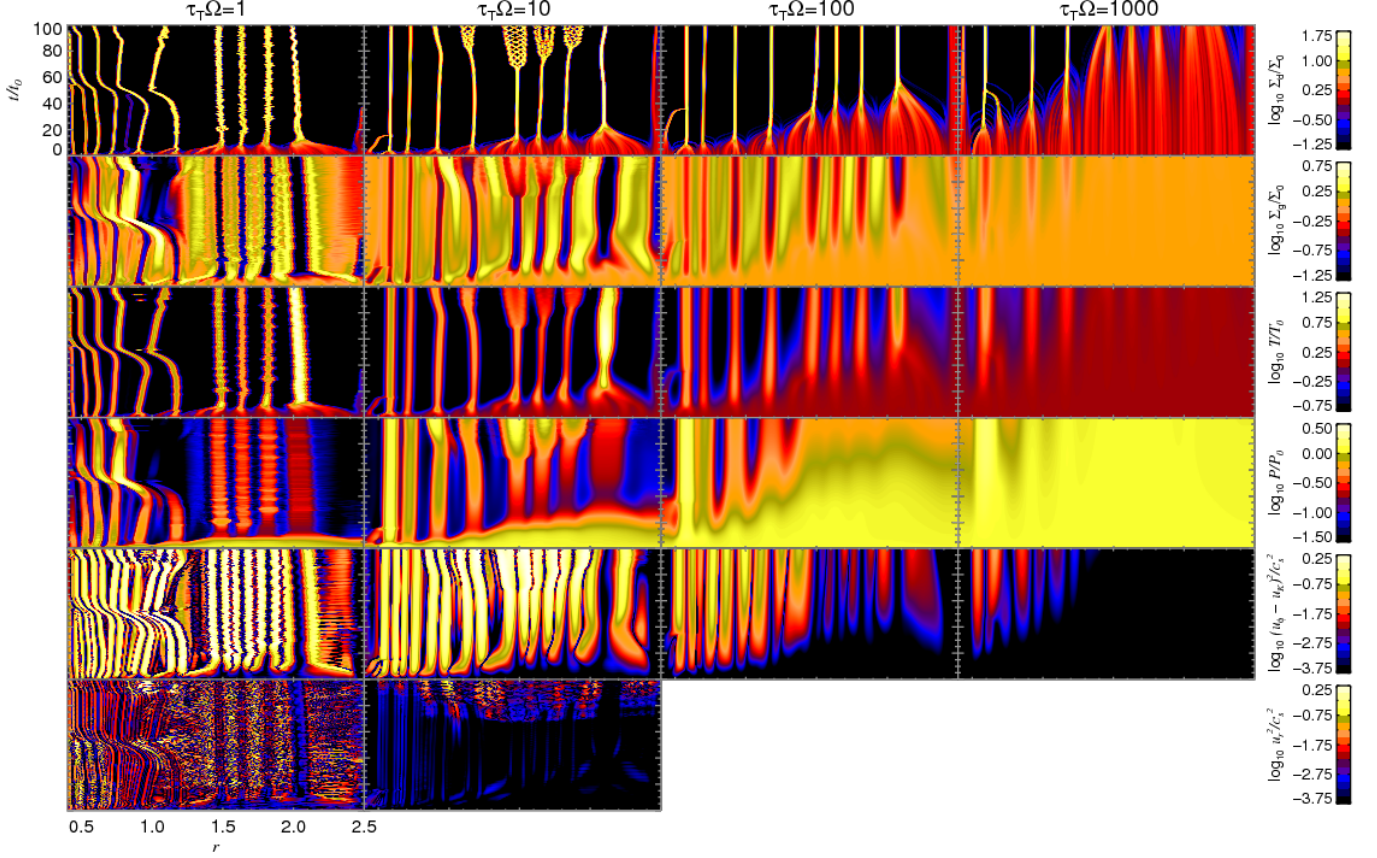


FIG. 7.— Parameter space exploration for the thermal coupling time τ_{T0} in models with $\tau_{f0}=1$ and without backreaction. The pressure build-up associated with too short thermal coupling time leads to modification of the centrifugal balance experienced by a gas parcel. In the case of $\tau_T=10$ the pressure buildup leads to supersonic motion and consequent disruption of the dust fingers into a turbulent pattern. The models with larger τ_{T0} are better behaved as the buildup is slow. After long enough times (not shown) they too develop shock waves that disturb the dust streams. The dynamics is considerably different in models including back-reaction (Fig. 9).

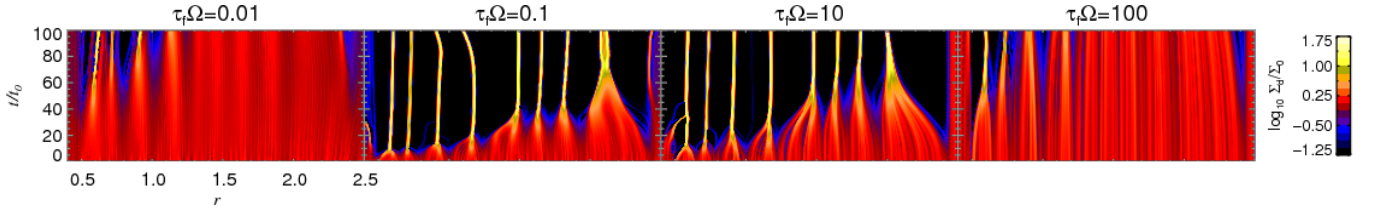


FIG. 8.— Parameter space exploration for the friction time τ_{f0} in models with $\tau_{T0}=10$ and without backreaction. There is an apparent symmetry with respect to $\tau_f = 1$. As the dust decouples (larger τ_f) the particles take longer times to move to the local pressure maxima. As the dust couples more strongly (lower τ_f), a grain longer times to move away from the density maxima (pressure minima) into the pressure maxima. The velocities never get too close to sonic so turbulent disruption as in the case of short thermal coupling time does not occur.

presence of gas, as shown later).

In Fig. 6 we show the radial profile of different quantities by the end of the simulation at 100 orbits (left panel), and their time evolution (right panel). This simulation has $\tau_T = 10$ and $\tau_f = 1$, i.e., a thermal coupling time of 10 orbits and a dynamical coupling time of 1 orbit. The initial random overdensities quickly grow into massive accumulations of dust. The dust heats up the gas, which is seen in the correlation between dust density and temperature. As a result of the heating, the gas expands, seen in the anti-correlation between gas density and temperature. Interestingly, this implies an anti-correlation between gas and dust densities. This behav-

ior has been predicted by Besla & Wu (2007). Rings or clumps of photoelectric emitting dust should thus be relatively gas-free. Conversely, dense rings and blobs of gas should be cold and relatively dust-free.

This highlights a difference between the present analysis and that of Klahr & Lin (2005). As those authors considered a time-independent gas density profile, the gas does not expand (compress) upon heating (cooling). Let us analyze if any qualitative difference should be expected due to expansion or compression.

5.3.2. Effect of pdV work

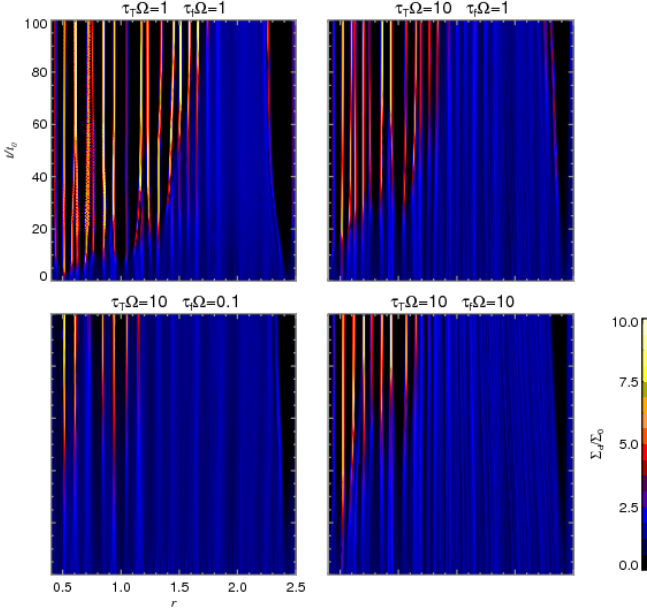


FIG. 9.— The effect of the backreaction of the drag force is illustrated above. The upper panels show the space-time variation of the dust density in models of constant friction time and varying thermal time. The lower panels show models of varying friction time and constant thermal time. Compared to the same models without backreaction (Fig. 7 and Fig. 8), we see that the dust streams are better shepherded. This is because when radial velocities are excited, the drag force backreaction damps them back to zero at an e-folding time $\tau_f \Sigma_g / \Sigma_d$. The shepherding of the dust stream should occur as long as this quantity is smaller or similar to τ_T .

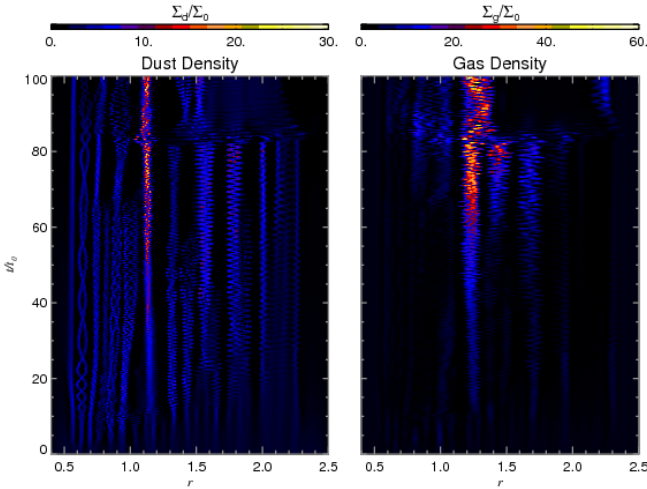


FIG. 10.— Model with instantaneous thermal coupling between gas and dust. The gas attains much denser concentrations, and the dust executes high frequency oscillations. At later times the dust streams in the outer disk break into a roughly uniform sheet of dust extending from $r=1.4$ to $r=2.0$.

The expansion occurs at the speed of sound, the characteristic timescale being therefore the sound crossing time. Because the structures formed are of size H (where $H = c_s / \Omega$ is the scale height), the sound crossing time equals the dynamic timescale $\tau_{\text{dyn}} = 1/\Omega$. We have therefore two timescales; the time scale of the thermal

coupling τ_T , and the timescale of the response of the gas, $1/\Omega$. Their ratio $\tau_T / \tau_{\text{dyn}} = \tau_T \Omega$ is a dimensionless number between the second and first terms in the right hand side of the entropy equation (Eq. 3), namely relaxation and advection. Hidden in the latter term is the pdV work. If $\tau_T \Omega$ is too big, relaxation is slow and advection dominates, i.e., the expansion is adiabatic. If on the other hand $\tau_T \Omega$ is too small, advection is slow and relaxation dominates. That means that the temperature changes faster than the gas can respond. The gas is unchanged and the process is therefore isochoric. So, schematically, the temperature rise from T_2 to T_1 will, in each regime, brings the pressure from P_1 to P_2 according to

$$\text{if } \tau_T \Omega \gg 1 \implies P_2 = P_1 (T_2/T_1)^{\gamma/(\gamma-1)} \quad (43)$$

$$\text{if } \tau_T \Omega \ll 1 \implies P_2 = P_1 (T_2/T_1) \quad (44)$$

and as $\gamma > 1$, p_2/p_1 and T_2/T_1 have the same sign, so a rise in temperature leads to a rise in pressure irrespectively of the density drop. The instability would only be quenched if the temperature rise occurred at constant pressure. This condition could only be fulfilled if the expansion occurred in a huge pressure reservoir, which is not the case of gas-poor debris disks. We are safe to state that the photoelectric heating of the gas will lead to pressure rise and further concentration of dust if the latter is mobile. We show this in Fig. 7, where models with the exploration of the parameter space for $\tau_T \Omega$ is shown. From left to right we show models of $\tau_T \Omega = 1, 10, 1000$, and 1000 . The friction time was kept constant at $\tau_f \Omega = 1$ so that the dust is mobile. In all cases the dust concentrates.

The models shown in Fig. 7 contain some interesting features worth highlighting. As seen in the model of $\tau_T \Omega = 1.0$, there are instances in time, around 30 orbits, that the dust distribution rapidly migrates inwards, setting in another equilibrium location. In the model with $\tau_T \Omega = 10$ the dust at later times, around 50 orbits, passes from a thin stream to a shower, resembling the transition to turbulence seeing in, e.g., cigarette smoke. Both effects seem to be related to the pressure buildup. As the dust concentrates, the local temperature rises, leading to further dust buildup. The runaway process has to saturate at some point, and these effects seem to be manifestations of saturation. The pressure buildup leads to a gradual change in the centrifugal equilibrium $r\dot{\phi}^2 = r\Omega_K^2 + \Sigma_g^{-1} \partial_r P$. At some point the buildup of pressure significantly changes that relation, and the disk readjusts. In the other case, the buildup of pressure leads to supersonic speeds. Shock waves develop, leading to the disruption of the dust stream. These effects will be significantly mitigated by the inclusion of the drag force backreaction, in Sect. 5.3.4.

5.3.3. Effect of gas drag

The models shown in the previous section were run with a fixed friction time of $\tau_f \Omega = 1$, representing the most mobile particles. We consider now models with varying τ_f , keeping $\tau_T \Omega = 10$. A suite of such models is shown in Fig. 8. As the dust decouples, it takes time for the pressure gradient to move the particles to the

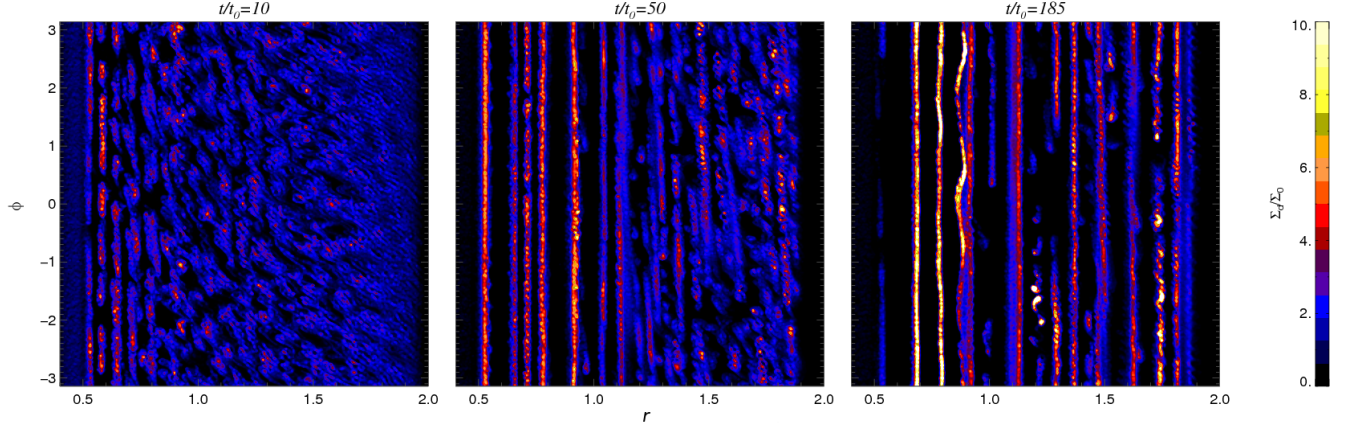


FIG. 11.— Snapshots of the dust density, at 10, 50, and 200 orbits, respectively. The heating-clumping instability concentrates the dust axis-symmetrically into rings. The axis-symmetric is due to strong damping of non-axisymmetric modes provided by the drag force backreaction. At latter times, one of these rings is seen to oscillate, appearing as an eccentric ring. This is not because of the presence of a eccentric planet shepherding the ring, but simply the result of a standing wave propagating along it.

pressure maxima. As the dust couples more strongly, it takes time for the dust to decouple itself from the density maxima (pressure minima) and into the pressure maxima. The symmetry with respect to $\tau_f \Omega = 1$ is striking.

In the extreme of particle tracers ($\tau_f = 0$) there is no instability as the gas and dust cannot get separated. The heating leads to expansion, that carries away the dust, leading to cooling. The process is self-regulated. In the opposite extreme of decoupled dust $\tau_f \rightarrow \infty$ there is no instability either as the dust does not get pushed toward pressure maxima.

5.3.4. Effect of gas drag back-reaction

We now turn to the effect of the last term in the right hand side of the momentum equation, the drag force backreaction from the particles onto the gas. We re-run models of $\tau_T \Omega = 1$ and 10, with $\tau_{f0} = 1$ (the leftmost ones in Fig. 7), but now including this term. The results are shown in the upper panels of Fig. 9, for the dust density only. Comparing these models with the ones without back-reaction shown in Fig. 7, we see that the jerks in position are absent, as well as the dispersion of the particles into turbulent streams as seen in the models without backreaction. In other words, the backreaction of the drag force has the effect of shepherding the dust streams.

The reason is because in the other models, although the dust is forced to follow the gas, the gas is unconstrained by the dust. When backreaction is included, the gas follows the dust whenever the dust-to-gas ratio ε is high. When $\varepsilon \gg 1$ the backreaction dominating the gas motion effectively herds the dust; a linear perturbation to the system executes exponentially damped oscillations, as discussed in Sect. 4.

Interestingly, this effect, being proportional to τ_f , should break the symmetry with respect to $\tau_f = 1$ seen in the models without backreaction (Fig. 8). Indeed, this is what is seen in the lower panels of Fig. 9, where we show the result of two simulations with $\tau_T = 10$ and back-reaction included, varying τ_f . The left panel has $\tau_f = 0.1$

and the right panel has $\tau_f = 10$. The simulation with shorter friction time experiences less clumping for the same thermal coupling time.

The herding provided by the drag force also introduces a dependency on τ_T / τ_f , because if $\tau_T \ll \tau_f$, the pressure builds much faster than the dust can respond. The backreaction becomes less important, and the situation becomes similar to the one shown in the left panels of Fig. 7.

5.3.5. A model with instantaneous thermal coupling

We test now models with instantaneous thermal coupling, where the equation of state is given by Eq. (10). The time evolution of the dust and gas densities is shown in Fig. 10. The evolution looks a hybrid between the models shown so far. On the one hand the dust streams are very thin, because of the shepherding provided by the drag force backreaction. On the other hand, the infinitesimally small thermal time leads to rapid wave excitation, seen in the high frequency oscillation of the dust. Interestingly, at later times, (< 80 orbits) the thin streams in the outer disk get disrupted and form a roughly uniform extended sheet of particles spanning $r = [1.4, 2.0]$, a significant part of the radial domain. A very dense concentration of gas ($\Sigma_g = 60$) occurs in the low-pressure dust void left by the massive particle concentration at $r = 1.2$.

5.3.6. The model in two dimensions

Having analyzed the behavior of the instability in 1D models, we turn our attention to two-dimensional models. We show in Fig. 11 snapshots of the disk at 10, 50, and 185 orbits. The appearance of the disk in Cartesian projection, for the last snapshot, is shown in Fig. 12. Though the initial distribution is clumpy, the system rearranges itself in rings, which suggests a damping of non-axisymmetric modes. We checked that in the absence of backreaction there is no development of rings - the system consists simply of clumps. This implies that it is the drag force backreaction that is providing the damping. The regular spacing of the rings, also seen

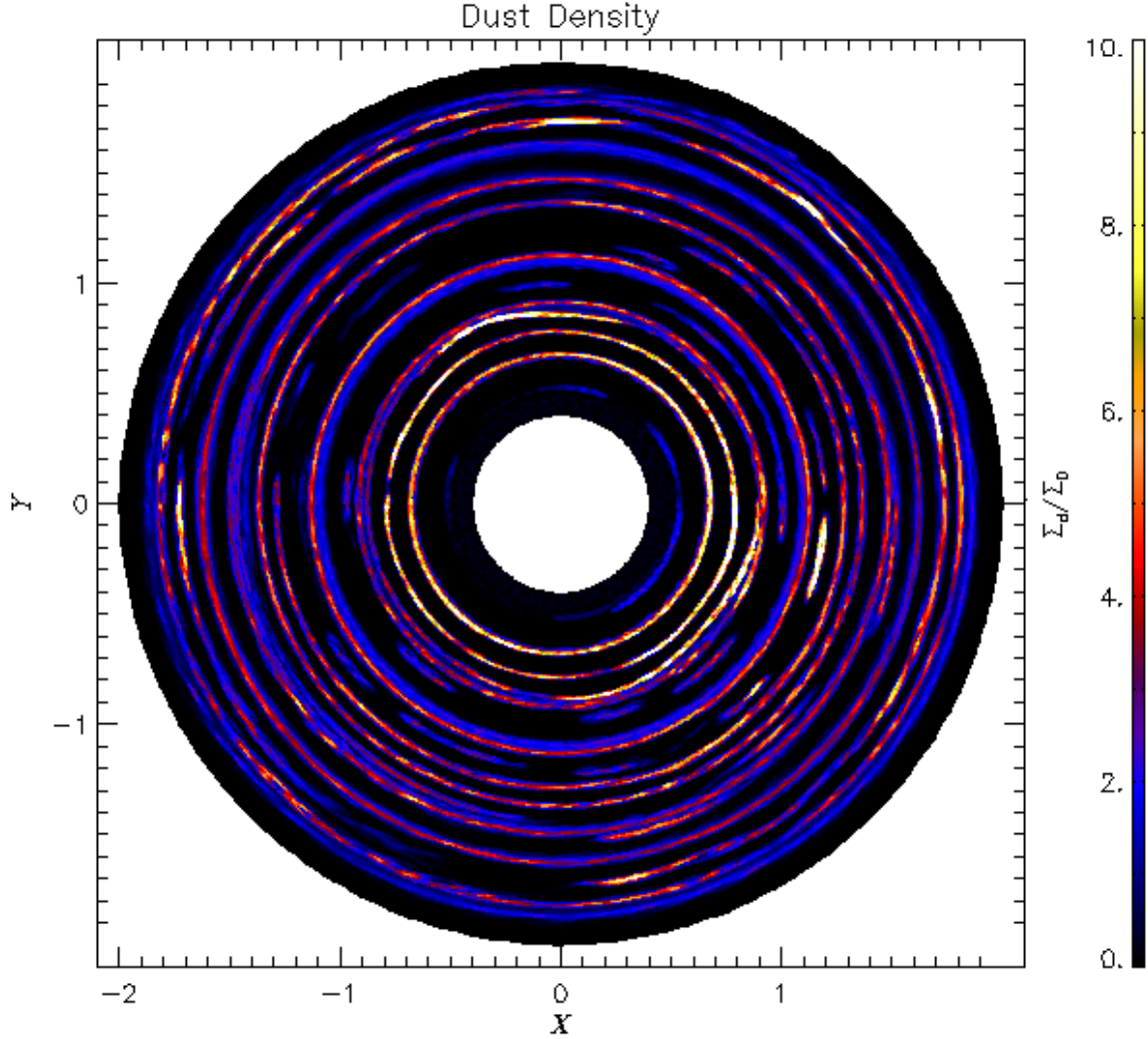


FIG. 12.— Appearance of the disk in Cartesian coordinates. An oscillation traveling along the ring between $r=0.8-0.9$ shows itself as deviations from axis-symmetry, at 4 and 11 o'clock. The eccentricity of the ring is $e = 0.04$, similar to the eccentricity observed in the debris disk around HD 61005.

in the one-dimensional models, speak of a preferred radial wavelength for the instability (though no hint of this most unstable wavelength was found in the linear stability analysis).

The most interesting development of the model, though, is seen in the rightmost panel of Fig. 11. At late times, one of the rings starts to oscillate. The oscillation does not grow in time, which shows that it is not an instability. In fact, as shown before, it is rather an epicycle executed in the orbital plane, with a period equaling the Keplerian period. The observational upshot is that the disk appears off-centered. In Fig. 13 we show this particular ring only. The location of the star $[x, y] = [0, 0]$ is marked with a red “x”. The dusty ansae appear offcentered, the lower one at minimum elongation $r_{\min}=0.84$, and the upper one at maximum elongation $r_{\max}=0.91$. These “apsides” are not exactly diametrically opposed. Though they are extended, we define

their azimuthal location as the azimuths of the points of minimum and maximum elongation, ϕ_{\max} and ϕ_{\min} , respectively. The “center” $[r_c, \phi_c]$ of the eccentric ring is thus at $r_c = (r_{\max} + r_{\min})/2$, the middle point in radius; and $\phi_c = (\phi_{\max} + \phi_{\min})/2$, the average between the azimuth of the outer ansa and the azimuth of (the antipode) of the inner ansa. This is marked as a black “x”. The eccentricity of the ring is

$$e = \frac{r_{\max} - r_{\min}}{r_{\max} + r_{\min}} = 0.04. \quad (45)$$

a value that matches the eccentricity found for the ring around HD 61005 ($e=0.045 \pm 0.015$, Buenzli et al. 2010). Though they fall short of the eccentricity of the Fomalhaut ring ($e = 0.11$, Kalas et al. 2005), larger amplitude oscillations could account for that eccentricity. The point to make is that a standing wave through a narrow

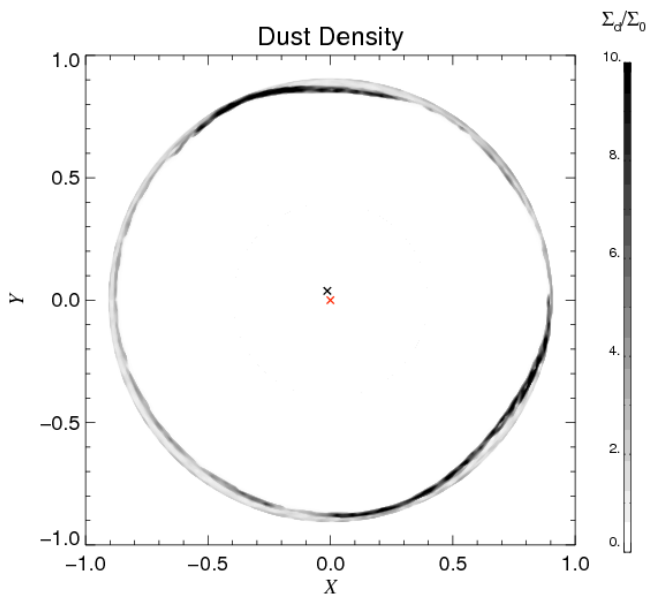


FIG. 13.— Appearance of the oscillating ring. The star and the center of the ring defined by the dusty ansae are marked red and black “x”, respectively. Due to the wave propagating along it, the ring appears off-centered, with eccentricity $e = 0.04$.

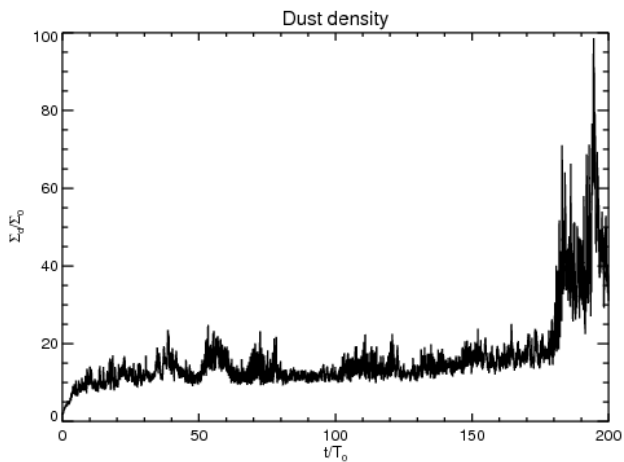


FIG. 14.— The maximum dust density in the model shown in Fig. 11. The peak near the end of the simulation is the bright dust clump located at $r \approx 1.2$ seen in the rightmost panel of Fig. 11. In actual images of debris disks, this clump could be bright enough to be mistaken for a planet shepherding a sharp eccentric ring.

ring is seen as eccentricity, a feature which is usually attributed to the gravitational influence of hypothetical undetected planets in eccentric orbits.

We also see that although axis-symmetry is strongly favored, some rings broke into clumps at later times. In the rightmost panel, at $t = 185$ orbits, the clumps at $r \approx 1.2$ achieved a very high dust load with $\Sigma_d/\Sigma_0 \approx 40$, sometimes exceeding 100 (see Fig. 14). This is interesting because these dust clumps are seen quite close to the borders of the narrow rings, and could be mistaken for a planet due to their brightness and compactness.

Indeed, this situation could explain the bright moving source in the debris disk around Fomalhaut. The source was initially thought to be a planet shepherding an eccentric sharp ring (Kalas et al. 2005), but that hypothesis was dealt a serious blow recently as the source could not be detected in the near infrared (Janson et al. 2012). The most likely explanation, as suggested by the authors, is an extended cold dust cloud shining through reflected light. Recent work by (Boley et al. 2012) suggests that the ring is confined by a pair of shepherding terrestrial mass planets, well below the current detection limits. Detection of gas around the ring would be a way to distinguish that scenario from the one we propose. At present, only upper limits on the amount of gas in the Fomalhaut system exist (Liseau 1999); they are relatively insensitive, however, because they probed CO emission, and CO could easily be dissociated around this early A type star.

We notice also that at times the ring displays multiple apsides, which means oscillations with higher frequency than simple epicycles. Undamped modes with $\omega \propto k$ appeared in the linear analysis for $\varepsilon = 1$ and, though the dust-to-gas ratio is not strictly unity in this dynamical case, similar undamped modes should account for this behavior.

We modeled also a $r - z$ slice of the disk, in order to investigate the vertical structure of the debris disk. The resolution is 256×128 , spanning $2H$ above and below the midplane, and $8H$ in the radial direction. Particles of three sizes were used, of friction times $\tau_f = 0.0, 0.1$ and 1.0 . The behavior of the particles resembles that in the simulations of Johansen et al. (2006) for particle settling in the midplane of protoplanetary disks. The more decoupled particles settle first, and stir the midplane into a mild Kelvin-Helmholtz turbulence that supports through diffusion a particle subdisk of finite thickness (Dubrulle et al. 1995; Garaud & Lin 2004). The difference in the debris disk case reflects the fact that the dust is the heating agent, so once the dust settles, the gas in the midplane starts to get heated up. This gas expands and eventually becomes buoyant. At later times, as seen in the rightmost panel of Fig. 15, the midplane of the disk develops significant voids of gas, that is pressed against the upper layers. This may account for the disparity found in the measured gas scale heights in the few debris disks where gas lines could be measured.

6. CONCLUSIONS

We modeled for the first time the hydrodynamics of debris disks. These disks are usually assumed to be gas-free, yet outgassing from planetesimals and dust grains should occur, supplying gas and maintaining a dust-to-gas ratio of roughly unity.

Heated by the star, the dust transfers the heat to the gas, which expands, contracting again in colder regions devoid of dust. An anti-correlation between dust and gas densities follows, which was not observed by (Klahr & Lin 2005). In one dimension, the system develops well-spaced spikes in dust density, that in two-dimensions assume the shape of well-defined, sharp rings. The sharpness is a consequence of the drag force backreaction, that efficiently damps high frequency oscillations at high dust load. This herding by the drag

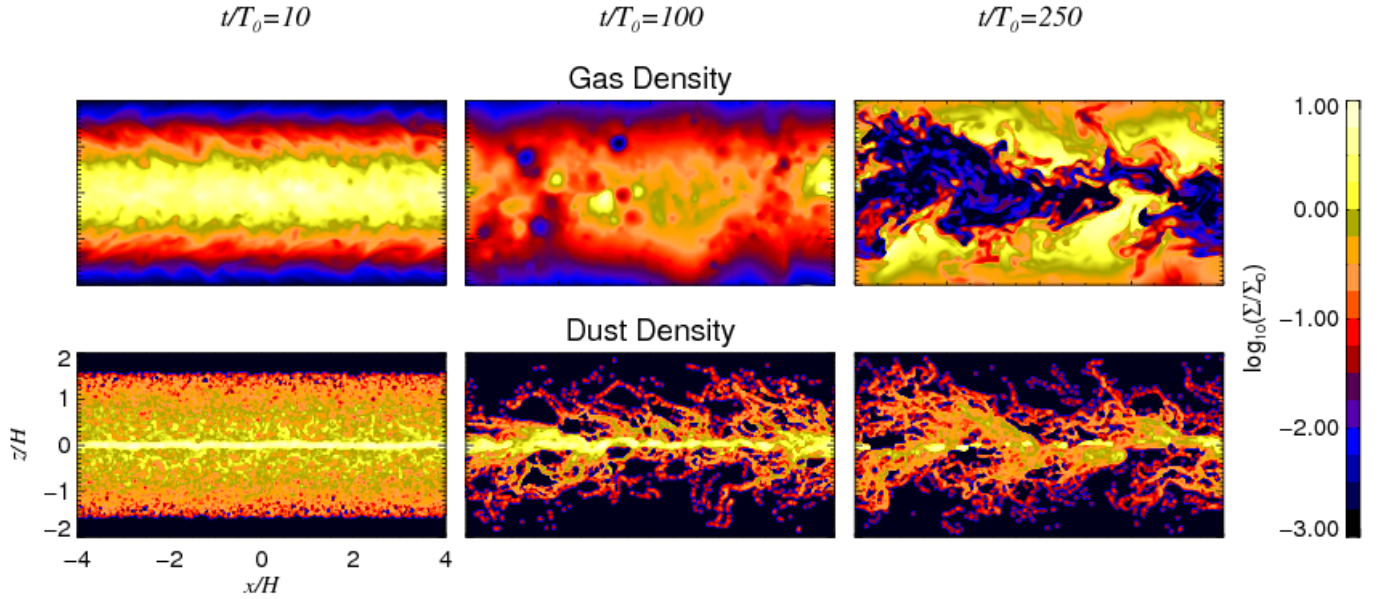


FIG. 15.— A simulation in the $r-z$ plane, in order to investigate the vertical structure of debris disks subject to the heating-clumping instability. The upper panels show the gas density, and the lower the dust density. Particles of three sizes are represented. The dust settles to the midplane, supported by self-sustained Kelvin-Helmholtz turbulence. It heats the gas in the midplane, that in turn expands. At later times, dust-gas segregation has been established, with the hot dust expelling the gas from the midplane.

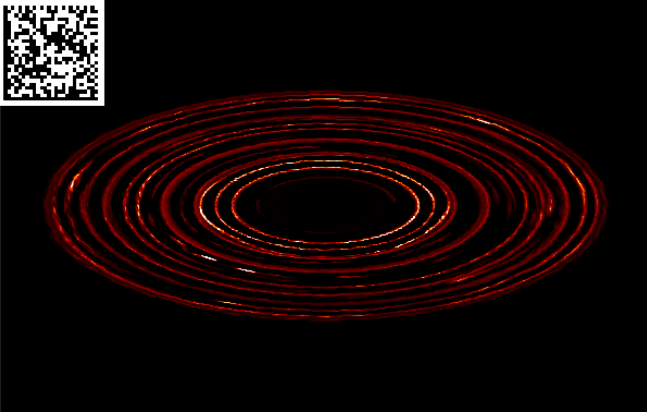


FIG. 16.— A snapshot of the model, inclined to the same orientation of the debris disks around Fomalhaut. The bright dots are high concentrations of dust, and would be very bright in reflected light. As they also move in Keplerian orbits, they could be easily mistaken for planets. Scan the barcode at the top left corner for an animation of the simulation.

force has not previously been accounted for, and may explain the sharp rings seen in actual images of debris disks. A snapshot of the model, rotated to the same inclination of the debris disk around Fomalhaut, is shown in Fig. 16.

The system supports a spectrum of oscillations, most of them damped by the drag force. However, some specific modes for which the gas and dust velocity coincide correspond to undamped oscillations. For these modes, the rings behave as wave guides. The visual result of these oscillations is a finite eccentricity. In our model, we measure $e = 0.04$ for one of the oscillating rings. This is in good agreement with the observed eccentricities of rings in debris disks. These eccentricities are usually presented as convincing evidence for

the presence of unseen planets in eccentric orbits, whose gravitational influence would shepherd the ring and impart its eccentricity to it. Our model explains both features without the need of a planet. The eccentricity is simply a standing wave propagating along the ring. This fits neatly with the recent (Janson et al. 2012) infrared non-detection from the bright source around Fomalhaut (Kalas et al. 2005), indicating that the source is most likely a dust cloud and not a planet shepherding the eccentric ring, as previously assumed. We notice that the possibility of these features arising from density waves instead of from gravitational influence of unseen companions has been raised by Jalali & Tremaine (2012). The difference between that work and the present one is that they ignored dust-gas interactions, relying on stellar encounters to trigger the density waves. We show instead that oscillations can arise through hydrodynamics, without the need for external perturbers.

We also model a $r-z$ slice of the disk, following the settling of the dust and how it impacts the gas. We find that the gas is expelled from the midplane. It presses against the gas above and below, increasing the gas density in the atmosphere. The vertical structure of debris disks is therefore hot thin gas in the midplane, cold dense gas above and below, as also previously suggested by Besla & Wu (2007). This highly unstable situation is maintained as long as the dust is present in the midplane.

We caution that the models presented are very simplified, and should be taken more as proofs of concepts than conclusive evidence. We plan in future publications to include magnetic fields, add a more realistic treatment of the disk thermodynamics, perform a full 3D analytical analysis and numerical calculations, and push the resolution to the limit of modern computational power. Still, that the simple models presented

here shed new light in pertinent unsolved questions of debris disks is an illustration of the importance of hydrodynamics in these systems.

The writing of this paper started at the American Museum of Natural History, with financial support by the National Science Foundation under grant no. AST10-09802, and completed at the Jet Propulsion Labora-

tory, California Institute of Technology, under a contract with the National Aeronautics and Space Administration. This research was supported by an allocation of advanced computing resources supported by the National Science Foundation. The computations were performed on the Kraken system at the National Institute for Computational Sciences. We acknowledge fruitful discussions with Glen Stewart and Henrik Latter.

REFERENCES

- Besla, G. & Wu Y. 2007, *ApJ*, 655, 528
 Boley, A. C., Payne, M. J., Corder, S., Dent, W. R. F., Ford, E. B., & Shabram, M. 2012, *ApJ*, 750, 21
 Brandeker, A., Liseau, R., Olofsson, G., & Fridlund, M. 2004, *A&A*, 413, 681
 Buenzli, E., Thalmann, C., Vigan, A., Boccaletti, A., Chauvin, G., Augereau, J. C., Meyer, M. R., Ménard, F., Desidera, S., Messina, S., Henning, Th., Carson, J., Montagnier, G., Beuzit, J. L., Bonavita, M., Eggenberger, A., Lagrange, A. M., Mesa, D., Mouillet, D., & Quanz, S. P. 2010, *A&A*, 524, 1
 Czechowski, A., & Mann, I. 2007, *ApJ*, 660, 1541
 Dubrulle, B., Morfill, G., & Sterzik, M., 1995, *Icarus*, 114, 237
 Garaud, P., & Lin, D. N. C. 2004, *ApJ*, 608, 1050
 Grigorieva, A., Thebault, P., Artymowicz, P., & Brandeker, A. 2007, *A&A*, 475, 755
 Jalali, M. A. & Tremaine, S. 2012, *MNRAS*, 421, 2368
 Janson, M., Carson, J. C., Lafrenière, D., Spiegel, D. S., Bent, J. R., & Wong, P. 2012, *ApJ*, 747, 116
 Johansen, A., Henning, Th., & Klahr H. 2006, *ApJ*, 643, 1219
 Kalas, P., Graham, J. R., & Clampin, M. 2005, *Nature*, 435, 1067
 Klahr, H. & Lin, D. N. C. 2005, *ApJ*, 632, 1113
 Lagrange, A. et al., 1998 *A&A*, 330, 1091
 Lesur, G. & Papaloizou, J. C. B., 2010, *A&A*, 513, 60
 Liseau, R. 1999, *A&A*, 348, 133
 Lyra, W. & Klahr, H. 2011, *A&A*, 527, 138
 Lyra, W., Johansen, A., Zsom, A., Klahr, H., & Piskunov, N. 2009, *A&A*, 497, 869
 Lyra, W., Johansen, A., Klahr, H., & Piskunov, N. 2008, *A&A*, 479, 883
 Maness, H. L., Fitzgerald, M.P., Paladini, R., et al. 2008, *ApJ*, 686, L25
 McNally, C. P., Lyra, W., & Passy, J.-C. 2012, arXiv:1111.1764
 Moor, A. et al. 2011, *ApJ*, submitted, (astro-ph/1109.2299)
 Olofsson, G., Liseau, R., & Brandeker, A. 2001, *ApJ*, 563, L77
 Redfield, S. 2007, *ApJ*, 656, L97
 Roberge, A., Feldman, P.D., Weinberger, A.J., Deleuil, M., & Bouret, J.-C. 2006, *Nature*, 441, 724
 Takeuchi, T. & Artymowicz, P. 2001, *ApJ*, 557, 990
 Thi, W.F., Blake, G.A., van Dishoeck, E.F. et al. 2001, *Nature*, 409, 60
 Troutman, M.R., Hinkle, K.H., Najita, J.R., Rettig, T.W. & Brittan, S.D. 2011, *ApJ*, 738, 12
 Zagorovsky, K., Brandeker, A., & Wu, Y. 2010, *N, ApJ*, 720 923
 Zuckerman, B., Forveille, T., & Kastner, J. H. 1995, *Nature*, 373, 494